A THREE-DIMENSIONAL IMAGING ALGORITHM FOR TOMOGRAPHY SAR BASED ON IMPROVED INTERPOLATED ARRAY TRANSFORM

X. Z. Ren[*], L. H. Qiao, and Y. Qin

College of Information Science and Engineering, Henan University of Technology, Zhengzhou, China

Abstract—The imaging quality of tomography SAR is limited by the low number of flight tracks and their non-uniform distribution. In this paper, a new 3-D imaging algorithm is proposed for tomography SAR based on the improved interpolated array transform. The key point of the proposed algorithm is the introduction of the projection technique into the interpolated array transform, which can reduce the energy of the interference signal and improve the imaging quality. Performance analysis under different scenarios is carried out via the simulations. And the results demonstrate that the sidelobe performance can be significantly improved by the proposed algorithm.

1. INTRODUCTION

Traditional synthetic aperture radar (SAR) systems can reconstruct 2-D images of the investigated area with all-weather capability [1–6]. However, 2-D images could not meet the requirements in many applications, and 3-D images are anticipated. Synthetic aperture radar interferometry (InSAR) technology is a powerful technique used to measure the elevation of the terrain patch [7–9], but the distribution of the scatterers in height is underdetermined and cannot be resolved by a single baseline measurement. As the extension of conventional InSAR, tomography SAR adds multiple baselines in the direction perpendicular to the azimuth and to the line of sight and forms an additional synthetic aperture in the height direction. Therefore, it has a resolving capability along this dimension [10].

Fourier transform method was first proposed to obtain the height image of tomography SAR; however, the height resolution is limited

by the low number of tracks [10]. Compared with the Fourier transform method, spatial spectrum estimation methods can obtain lower sidelobes and higher resolution in the height direction [11], but which suffered from high sidelobes under the non-uniform track distribution. Excessively non-uniform passes may lead to completely unsatisfactory reconstruction with high ambiguity levels.

To overcome these difficulties, an accurate focused algorithm was proposed based on backprojection [12], which suffered from severe computational complexity. Subsequently, also singular value decomposition method was considered to focus the non-uniform data in the height direction [13]. An additional problem is that this method should handle an ill-conditioning inverse problem. In a recent work, the sector interpolation method was applied to SAR tomography [14, 15], providing a beneficial effect on the imaging quality. However, the sidelobe performance can be improved comparing with the ideal data.

The main topic of this paper is to present a 3-D imaging algorithm for tomography SAR by introducing the projection technique into the interpolated array transform. As the first step, the virtual uniform array data can be acquired from the non-uniform one by the interpolated array transform. Then, the projection technique is used to project the steering vector of the virtual array into the signal subspace. This step can reduce the energy of the interference signal and improve the sidelobe performance. Afterwards, the height image can be acquired by beamforming. The rest of the paper is organized as follows. Section 2 presents the geometric and signal model of tomography SAR. The basic interpolated array transform method is introduced in Section 3. In Section 4, a new imaging approach is described in detail based on improved interpolated array transform. The performance of the method is investigated by simulated data in Section 5. Section 6 gives a brief conclusion.

2. TOMOGRAPHY SAR

Figure 1 shows the geometry of tomography SAR. x and y denote the range and azimuth directions, respectively. There are K passes over the same illuminated area. The interval between two pass is b, and the baseline length B is defined as the distance between the first and the last passes. ε is the angle between the baseline and the horizontal. The observation on the first pass is defined as the reference position with elevation H. Its look angle in the center of beam is θ, and its line of sight is the slant range direction, which is marked as r. The direction perpendicular to the azimuth and to the slant range is defined as the height direction, which is marked as s. Therefore, the 3-D
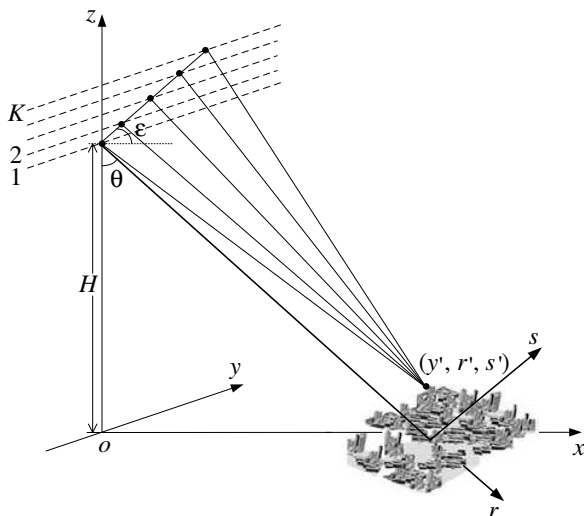
Figure 1. The geometry of tomography SAR.

imaging coordinates *y-r-s* are built, and the origin is at the position of the referenced observation. In each pass, the radar moves along the azimuth direction and transmits coherent phase modulated pulses in the range direction.

One 2-D SAR image is derived by one pass, and then K SAR images are derived by K passes. Suppose that all SAR images have been coregistered first, and then, the azimuth and slant range positions of each scatterer in all SAR images are the same. Because the interval between two pass is far less than the distance between the pass and the illuminated area, the K phase centers of tomography SAR can be aligned to form a linear array [16]. Therefore, the complex amplitudes of the pixels from the same azimuth-slant range resolution cell collected at the K phase centers of tomography SAR can be modeled as

$$\mathbf{y}(n) = \sum_{m=1}^{N_s} \sqrt{\tau_m} \mathbf{x}_m(n) \odot \mathbf{a}(\varphi_m) + \mathbf{v}(n), \quad n = 1, 2, \dots, N \quad (1)$$

where $\mathbf{y}(n)$, $\mathbf{x}_m(n)$, $\mathbf{a}(\varphi_m)$, and $\mathbf{v}(n)$ are K-dimensional complex vectors, n denotes the look index, N is the number of looks, $\odot$ is Hadamard product, and N_s is the number of backscattering sources. τ_m is the radar reflectivity of the mth sources. $\{\mathbf{x}_m(n)\}_{n=1}^N$ are the speckle complex vectors pertinent to the mth source, and $\mathbf{v}(n)$ is Gaussian thermal noise with zero mean and power σ_v^2 [16]. φ_m is the interferometric phase at the overall baseline, and $\mathbf{a}(\varphi_m)$ is the steering

vector for the mth source, which can be written as

$$\mathbf{a}(\varphi_m)$$
$$= \left[e^{j(b_{\perp 1}/B)\varphi_m}, e^{j(b_{\perp 2}/B)\varphi_m}, \ldots, e^{j(b_{\perp k}/B)\varphi_m}, \ldots, e^{j(b_{\perp K}/B)\varphi_m} \right]^T \quad (2)$$

where $b_{\perp k}$ is the orthogonal baseline of the kth phase center, B is the overall orthogonal baseline, and $(*)^T$ denotes the transpose operator.

The baseline interval is identical under ideal condition; hence the $b_{\perp k}$ can be written as

$$b_{\perp k} = \frac{k-1}{K-1} B \quad (3)$$

Replacing the $b_{\perp k}$ by (3) in Equation (2), the steering vector under ideal condition can be written as

$$\bar{\mathbf{a}}(\varphi_m) = \left[1, e^{j\varphi_m/K-1}, e^{j2\varphi_m/K-1}, \ldots, e^{j\varphi_m} \right]^T \quad (4)$$

Moreover, the interferometric phase φ_m is related to the spatial frequency w_m as $\varphi_m = (K-1)w_m$, and to the elevation angle θ_m as $\varphi_m = (K-1)w_m = 4\pi B \cos(\varepsilon - \theta_m)/\lambda$, where λ is the radar wavelength, and ε is the baseline tilt.

Based on the analysis of above, the scatterers in height of tomography SAR can be considered as the sources of the linear array. Therefore, the estimation of the different heights of the signals backscattered from the same azimuth-slant range resolution cell corresponds to estimate the interferometric phases $\{\varphi_m\}_{m=1}^{N_s}$ and the radar reflectivities $\{\tau_m\}_{m=1}^{N_s}$, spatial spectrum estimation methods can be adopted to obtain the height images. Unfortunately, for the current SAR tomography, it is almost impossible to avoid a non-uniform track distribution. This results in a poor imaging quality with the spatial spectrum estimation methods.

3. INTERPOLATED ARRAY TRANSFORM

The main idea of the interpolated array transform approach is dividing the field of view of the array into several sectors. The size of the sectors depends on the array geometry and desired accuracy [17–19]. For example, suppose the signal components belong to a sector Θ

$$\Theta = \begin{bmatrix} \varphi_1 & \varphi_2 & \varphi_3 & \ldots & \varphi_l \end{bmatrix} \quad (5)$$

where φ_1 and φ_l are the left and right borders of Θ, and the sampling occurs with a step defined by $\Delta\varphi = (\varphi_l - \varphi_1)/(l-1)$.

Form (2) the steering vector matrix of the real array can be written as

$$\mathbf{A} = \begin{bmatrix} \mathbf{a}(\varphi_1) & \mathbf{a}(\varphi_2) & \mathbf{a}(\varphi_3) & \ldots & \mathbf{a}(\varphi_l) \end{bmatrix} \quad (6)$$

where $\mathbf{a}(*)$ is a K-dimensional complex vector.

Form (4) the steering vector matrix of the virtual uniform array can be written as

$$\bar{\mathbf{A}} = [\bar{\mathbf{a}}(\varphi_1) \quad \bar{\mathbf{a}}(\varphi_2) \quad \bar{\mathbf{a}}(\varphi_3) \quad \ldots \quad \bar{\mathbf{a}}(\varphi_l)] \tag{7}$$

where $\bar{\mathbf{a}}(*)$ is a K_v-dimensional complex vector, and K_v is the number of the phase centers in the virtual array.

Then, the transformation matrix to transform the real array into the virtual array can be found as the solution of the following optimization problem

$$\mathbf{H} = \arg \min_{\mathbf{H}} \left\| \bar{\mathbf{A}} - \mathbf{H}^H \mathbf{A} \right\|_F^2 \tag{8}$$

where $\| * \|_F$ and $(*)^H$ denote the Frobenius norm and the Hermitian transpose, respectively.

Suppose that the $l > K$, the transformation matrix can be acquired by (8)

$$\mathbf{H} = \left(\mathbf{A}\mathbf{A}^H \right)^{-1} \mathbf{A}\bar{\mathbf{A}}^H \tag{9}$$

And the error of the interpolation can be defined as [17]

$$\mathbf{E}_{IA} = \frac{\left\| \bar{\mathbf{A}} - \mathbf{H}^H \mathbf{A} \right\|_F^2}{\left\| \bar{\mathbf{A}} \right\|_F^2} \tag{10}$$

Therefore, the output of the virtual array after the interpolated array transform is given by

$$\bar{\mathbf{y}}(n) = \mathbf{H}^H \mathbf{y}(n) \tag{11}$$

Moreover, the covariance matrix of the virtual array can be obtained from (1) and (11)

$$\bar{\mathbf{R}}_{\mathbf{y}} = E\left\{ \bar{\mathbf{y}}(n)\bar{\mathbf{y}}^H(n) \right\} = \mathbf{H}^H E\left\{ \mathbf{y}(n)\mathbf{y}^H(n) \right\} \mathbf{H}$$

$$= \sum_{m=1}^{N_s} \tau_m \mathbf{H}^H \mathbf{A}_m \mathbf{R}_{xm} \mathbf{A}_m^H \mathbf{H} + \sigma_v^2 \mathbf{H}^H \mathbf{H} \tag{12}$$

where $\mathbf{A}_m = \mathrm{diag}\{\mathbf{a}(\varphi_m)\}$, and the autocorrelation function of the speckle complex vectors $\{\mathbf{x}_m(n)\}_{n=1}^N$ can be given by [16]

$$\mathbf{R}_{xm}(u,v) = E\left\{ [\mathbf{x}_m(n)]_u \cdot [\mathbf{x}_m(n)]_v^* \right\}$$

$$= \begin{cases} 1 - \frac{|u-v|}{K-1} b_m, & |u-v| \le (K-1)/b_m \\ 0 & \text{others} \end{cases} \tag{13}$$

where $b_m = B_\perp / B_{\perp cm}$ is the normalized baseline of the mth source, $B_\perp$ is the baseline orthogonal to the line of sight, and $B_{\perp cm}$ is the normalized critical baseline of the mth source.

Moreover, from (8) we can get that

$$\mathbf{H}^H \mathbf{A}_m \approx \bar{\mathbf{A}}_m \tag{14}$$

Then, substituting (14) into (12) yields

$$\bar{\mathbf{R}}_\mathbf{y} \approx \sum_{m=1}^{N_s} \tau_m \bar{\mathbf{A}}_m \mathbf{R}_{xm} \bar{\mathbf{A}}_m^H + \sigma_v^2 \mathbf{H}^H \mathbf{H} \tag{15}$$

Consequently, the beamforming estimator after the interpolated array transform can be written as

$$\mathbf{P}(\varphi) = \frac{\bar{\mathbf{a}}^H(\varphi) \bar{\mathbf{R}}_\mathbf{y} \bar{\mathbf{a}}(\varphi)}{K_v^2} \tag{16}$$

4. IMPROVED INTERPOLATED ARRAY TRANSFORM

The idea of the improved method is to introduce the projection technique into the interpolated array transform, which can improve the sidelobe performance significantly.

Suppose the signal components belong to sector Θ, the correlation matrix of the virtual steering vector in the signal field can be defined as

$$\mathbf{R}_\Theta = \int_\Theta \bar{\mathbf{a}}(\theta) \bar{\mathbf{a}}^H(\theta) d\theta \tag{17}$$

Computing the eigenvalue decomposition of $\mathbf{R}_\Theta$ yields

$$\mathbf{R}_\Theta = \sum_{k=1}^{K_v} \lambda_k \mathbf{u}_k \mathbf{u}_k^H \tag{18}$$

where $\{\lambda_k\}_{k=1}^{K_v}$ are the eigenvalues of the matrix R_Θ, and $\lambda_1 \geq \lambda_2 \geq \ldots \geq \lambda_{K_v}$. $\mathbf{u}_k$ is the eigenvector corresponding to the eigenvalue λ_k.

Then, the projection matrix can be formed by the eigenvectors corresponding to the d largest eigenvalues

$$\mathbf{T} = \sum_{k=1}^{d} \mathbf{u}_k \mathbf{u}_k^H \tag{19}$$

Then, the projection transform is implemented to the steering vector matrix of the virtual array using the projection matrix $\mathbf{T}$

$$\tilde{\mathbf{A}} = \mathbf{T}\bar{\mathbf{A}} = \mathbf{T}\mathbf{H}^H \mathbf{A} = [\tilde{\mathbf{a}}(\varphi_1) \quad \tilde{\mathbf{a}}(\varphi_2) \quad \tilde{\mathbf{a}}(\varphi_3) \quad \ldots \quad \tilde{\mathbf{a}}(\varphi_l)] \tag{20}$$

where $\tilde{\mathbf{a}}(*)$ is a K_v-dimensional complex vector.

Therefore, the output of the virtual array after the projection transform can be written as

$$\tilde{\mathbf{y}}(n) = \mathbf{TH}^H \mathbf{y}(n) \tag{21}$$

Moreover, the covariance matrix of the virtual array after the projection transform can be rewritten as

$$\tilde{\mathbf{R}}_{\mathbf{y}} = \mathbf{TH}^H E\left\{\mathbf{y}(n)\mathbf{y}^H(n)\right\}\mathbf{HT}^H$$

$$= \sum_{m=1}^{N_s} \tau_m \mathbf{TH}^H \mathbf{A}_m \mathbf{R}_{xm} \mathbf{A}_m^H \mathbf{HT}^H + \sigma_v^2 \mathbf{TH}^H \mathbf{HT}^H \tag{22}$$

Then, substituting (20) into (22) yields

$$\tilde{\mathbf{R}}_{\mathbf{y}} = \sum_{m=1}^{N_s} \tau_m \tilde{\mathbf{A}}_m \mathbf{R}_{xm} \tilde{\mathbf{A}}_m^H + \sigma_v^2 \mathbf{TH}^H \mathbf{HT}^H \tag{23}$$

where $\tilde{\mathbf{A}}_m = \operatorname{diag}\{\tilde{\mathbf{a}}(\varphi_m)\}$.

It is obvious that the projection transform is used to project the covariance matrix of the virtual array into the signal subspace, which can reduce the energy of the interference signal and improve the estimation performance.

Moreover, from (9) and (19) we can get that $\mathbf{TH}^H \mathbf{HT}^H \neq \mathbf{I}$. That is to say, the noise has been colored noise after the interpolation and the projection transform, and the noise pre-whitening is required. Therefore, the output of the virtual array after the noise pre-whitening is [17]

$$\tilde{\mathbf{y}}_1(n) = \left(\mathbf{TH}^H \mathbf{HT}^H\right)^{-1/2} \mathbf{TH}^H \mathbf{y}(n) = \mathbf{Q}^{-1} \mathbf{TH}^H \mathbf{y}(n) \tag{24}$$

where $\mathbf{Q} = (\mathbf{TH}^H \mathbf{HT}^H)^{1/2}$.

Meanwhile, the covariance matrix of the virtual data becomes

$$\tilde{\mathbf{R}}_{\mathbf{y}_1} = \sum_{m=1}^{N_s} \tau_m \mathbf{Q}^{-1} \tilde{\mathbf{A}}_m \mathbf{R}_{xm} \tilde{\mathbf{A}}_m^H \mathbf{Q}^{-1} + \sigma_v^2 \mathbf{I} \tag{25}$$

And the beamforming estimator after the improved interpolated array transform can be written as

$$\mathbf{P}(\varphi) = \frac{\tilde{\mathbf{a}}^H(\varphi)\tilde{\mathbf{R}}_{\mathbf{y}_1}\tilde{\mathbf{a}}(\varphi)}{K_v^2} \tag{26}$$

5. SIMULATION RESULTS

In this section, to verify the validity of the proposed imaging algorithm for tomography SAR, the height dimensional imaging experiments and point-target simulation are carried out, respectively.

5.1. The Height Dimensional Imaging Results

First of all, suppose that there is a single source located at zero height with a signal-to-noise ratio of 12 dB, and there are five non-uniformly spaced tracks over the same illuminated area. Since we assumed the first phase center as the master track, the baseline intervals of each track related to the master track can be written as [0, 2, 5, 8, 9]b, where b is the reference baseline interval. This non-uniform baseline distribution can be obtained by thinning a 10-element full uniform array. Therefore, the improved interpolated array transform method can be used to obtain the height image of tomography SAR. From [16] we can get that the height unambiguous range of 10-element full uniform array extends from −4.5 to 4.5 height resolution units. If the interest signal range spans 5 height resolution units, and the height image obtained by the improved interpolated array transform method is plotted in Figure 2(a). In order to analyze the performance of the proposed method, the imaging results obtained by the non-uniform linear array data and the interpolated array transform method are also given for comparison in this and the following experiments. Moreover, the left and right borders of the signal range are presented by two solid beelines; the curves labeled with NLA are those obtained by the non-uniform array data, the curves labeled with IAT are those obtained by the interpolated array transform method, and the curves labeled with improved IAT are those obtained by the proposed method in this and the following figures. From Figure 2(a) we can get that the interpolation step has a beneficial effect on the sidelobes,
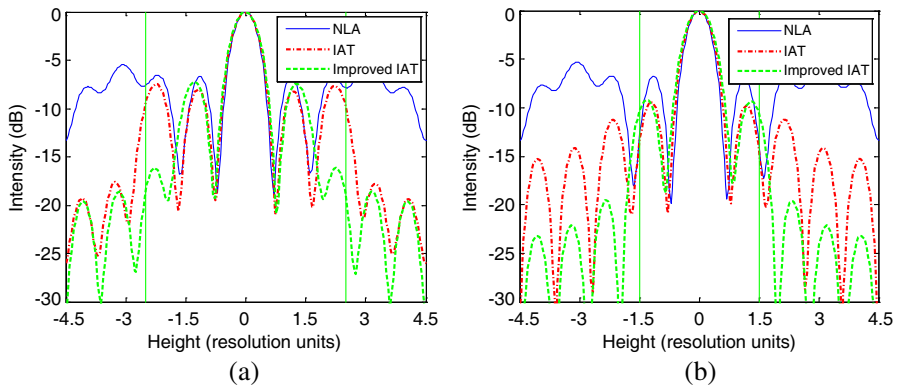

Figure 2. Height imaging results of tomography SAR with baseline intervals [0, 2, 5, 8, 9]b. (a) Signal range of 5 height resolution units. (b) Signal range of 3 height resolution units.

but the imaging result can be improved with a lower sidelobes after the projection transform. Maintaining the same array structure, Figure 2(b) shows the imaging results with a smaller signal range of 3 height resolution units. It is obvious that a narrower signal range would acquire a better reduction of the sidelobes.

The following case studies a more realistic geometry with eleven non-uniformly spaced tracks. The baseline intervals of each track related to the master track are [0, 2, 2.96, 4, 5.024, 5.92, 8.04, 9.04, 10.12, 12, 16.52]b, which can be obtained by thinning a 19-element full uniform array. The height unambiguous range of the 19-element full uniform array extends from -9 to 9 height resolution units. The height image obtained by the improved interpolated array transform method is plotted in Figure 3(a), with a signal range of 10 height resolution units. The imaging results confirm that the proposed method can handle a non-integer track structure and exhibit much better sidelobes behavior than the basic interpolated array transform method. Maintaining the same array structure, Figure 3(b) shows the imaging results with a smaller signal range of 6 height resolution units. As expected, it shows a better reduction of the sidelobes than that of Figure 3(a).

The coming to analysis takes into account two sources. The two sources are centered on zero height with a signal-to-noise ratio of 12 dB each, and distant 3 height resolution units. The baseline structure used in this experiment is the same as in Figure 3. The height image obtained by the improved interpolated array transform method
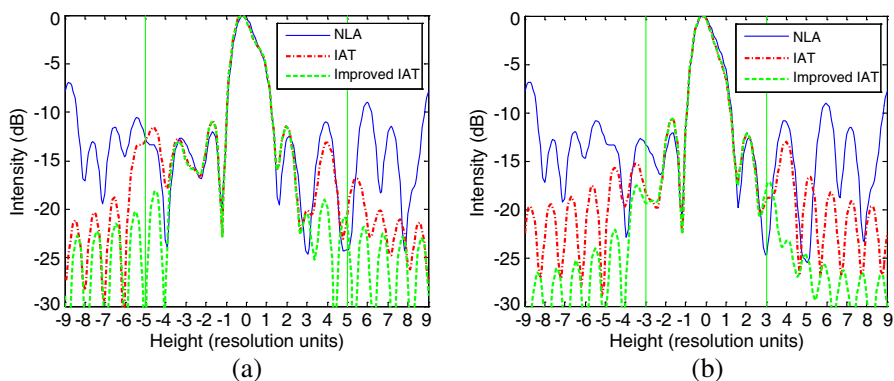

Figure 3. Height imaging results of tomography SAR with baseline intervals [0, 2, 2.96, 4, 5.024, 5.96, 8.04, 9.04, 10.12, 12, 16.52]b. (a) Signal range of 10 height resolution units. (b) Signal range of 6 height resolution units.
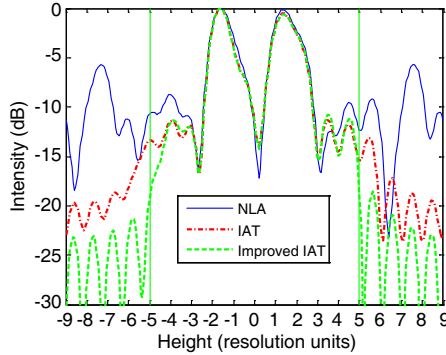
Figure 4. Height imaging results of tomography SAR with two sources.

Table 1. Parameters used for simulation.

Parameters	Value
Carrier frequency	1.3 GHz
Pulse bandwidth	75 MHz
Chirp duration	5.0 µs
Center of ground range	5000 m
Flight height	5000 m
Radar velocity	200 m/s
Baseline	400 m
Number of flight pass	21

is plotted in Figure 4, with a signal range of 10 height resolution units. Again, the proposed method provides a better profile extraction with a sidelobes reduction.

5.2. The Three-dimensional Imaging Results

To validate the proposed imaging algorithm, point targets are simulated in the last case. The azimuth-slant range-height coordinates of them are $(-30, 7054, \pm 8.5)$, $(-30, 7072, \pm 8.5)$, $(0, 7063, 0)$, $(30, 7054, \pm 8.5)$, and $(30, 7072, \pm 8.5)$. The main parameters used for simulation are listed in Table 1. The spatial baseline distribution is non-uniform, shown in Figure 5(a).

After raw-data generation and 3-D imaging processing of tomography SAR using the proposed method, the surfaces of the final 3-D image are shown at -3 dB in Figure 5(b). As expected, the image is well focused in the three directions.
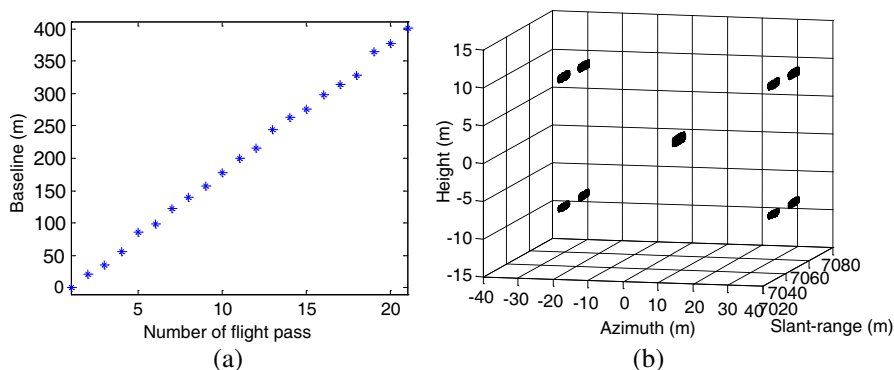
Figure 5. Spatial baseline distribution and final 3-D image. (a) Spatial baseline distribution. (b) Final 3-D image.
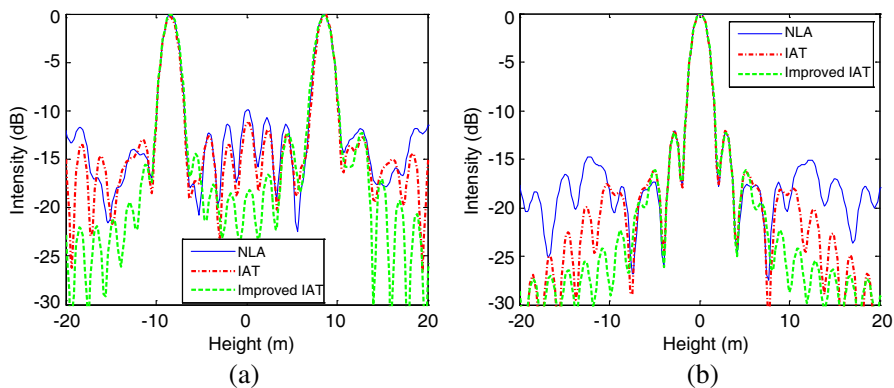

Figure 6. Height distributions of selected point targets. (a) Azimuth-slant range unit of $(-30, 7054)$. (b) Azimuth-slant range unit of $(0, 7063)$.

In order to analyze the performance of the imaging result, Figure 6 shows the height distributions of the point targets located in the azimuth-slant range units of $(-30, 7054)$ and $(0, 7063)$, respectively. And then, the imaging results are compared with the results obtained by the non-uniform sampling data and the interpolated array transform method. It can be seen clear that the proposed method shows a better sidelobes reduction capability and gives a better reconstruction quality.

6. CONCLUSIONS

In this paper, a new 3-D imaging algorithm that is capable of focusing tomography SAR data has been proposed. The principle behind the

method is based on considering the reduction of the energy of the interference signal thought projecting the steering vector into the signal subspace. The height dimensional imaging experiments with different scenarios and raw data of tomography SAR in L-band were simulated and the focused images were achieved by the proposed method. Meanwhile, the imaging results were compared with the non-uniform sampling data and the interpolated array transform method. The results of the simulated data confirm the effectiveness of the proposed method.

ACKNOWLEDGMENT

REFERENCES

1. Chan, Y. K. and V. C. Koo, "An introduction to synthetic aperture radar (SAR)," *Progress In Electromagnetics Research B*, Vol. 2, 27–60, 2008.

2. Lim, S.-H., J.-H. Han, S.-Y. Kim, and N.-H. Myung, "Azimuth beam pattern synthesis for airborne SAR system optimization," *Progress In Electromagnetics Research*, Vol. 106, 295–309, 2010.

3. Wei, S. J., X. L. Zhang, J. Shi, and G. Xiang, "Sparse reconstruction for SAR imaging based on compressed sensing," *Progress In Electromagnetics Research*, Vol. 109, 63–81, 2010.

4. Tian, B., D.-Y. Zhu, and Z.-D. Zhu, "A novel moving target detection approach for dual-channel SAR system," *Progress In Electromagnetics Research*, Vol. 115, 191–206, 2011.

5. Chang, Y.-L., C.-Y. Chiang, and K.-S. Chen, "SAR image simulation with application to target recognition," *Progress In Electromagnetics Research*, Vol. 119, 35–57, 2011.

6. Zhang, M., Y. W. Zhao, H. Chen, and W. Q. Jiang, "SAR image simulation for composite model of ship on dynamic ocean scene," *Progress In Electromagnetics Research*, Vol. 113, 395–412, 2011.

7. Wu, B.-I., M. C. Yeuing, Y. Hara, and J. A. Kong, "InSAR height inversion by using 3-D phase projection with multiple baselines," *Progress In Electromagnetics Research*, Vol. 91, 173–193, 2009.

8. Li, C. and D.-Y. Zhu, "A residue-pairing algorithm for InSAR phase unwrapping," *Progress In Electromagnetics Research*, Vol. 95, 341–354, 2009.

9. Liu, D., Y. Du, G. Sun, W.-Z. Yan, and B.-I. Wu, "Analysis of InSAR sensitivity to forest structure based on radar scattering model," *Progress In Electromagnetics Research*, Vol. 84, 149–171, 2008.

10. Reigber, A. and A. Moreira, "First demonstration of airborne SAR tomography using multibaseline L-band data," *IEEE Transactions on Geoscience and Remote Sensing*, Vol. 38, No. 5, 2142–2150, 2000.

11. Lombardini, F. and A. Reigber, "Adaptive spectral estimation for multibaseline SAR tomography with airborne L-band data," *IEEE International Geoscience and Remote Sensing Symposium 2003*, 2014–2016, Toulouse, France, 2003.

12. Ren, X. Z., X. F. Yin, R. L. Yang, and W. D. Yu, "A three-dimensional imaging algorithm for tomography SAR," *IEEE International Geoscience and Remote Sensing Symposium 2009*, 184–187, Cape Town, South Africa, 2009.

13. Fornaro, G., F. Serafino, and F. Soldovieri, "Three-dimensional focusing with multipass SAR data," *IEEE Transactions on Geoscience and Remote Sensing*, Vol. 41, No. 3, 507–517, 2003.

14. Lombardini, F., M. Pardini, and F. Gini, "Sector interpolation for 3D SAR imaging with baseline diversity data," *IEEE 2007 Waveform Diversity and Design Conference*, 297–301, Pisa, Italy, 2007.

15. Lombardini, F. and M. Pardini, "First experiment of sector interpolated SAR tomography," *IEEE International Geoscience and Remote Sensing Symposium 2010*, 21–24, 2010.

16. Gini, F., F. Lombardini, and M. Montanari, "Layover solution in multibaseline SAR interferometry," *IEEE Transactions on Aerospace and Electronic Systems*, Vol. 38, No. 4, 1344–1356, 2002.

17. Martorella, M. and B. Litileton, "Multibaseline cross-track SAR interferometry using interpolated arrays," *IEEE Transactions on Aerospace and Electronic Systems*, Vol. 41, No. 4, 1472–1481, 2005.

18. Yang, P., F. Yang, Z.-P. Nie, B. Li, and X. Tang, "Robust adaptive beamformer using interpolation technique for conformal antenna array," *Progress In Electromagnetics Research B*, Vol. 23, 215–228, 2010.

19. Yang, P., F. Yang, and Z.-P. Nie, "DOA estimation with sub-array divided technique and interpolated esprit algorithm on a cylindrical conformal array antenna," *Progress In Electromagnetics Research*, Vol. 103, 201–216, 2010.